Nanoscale

PAPER

View Article Online
View Journal | View Issue

Cite this: *Nanoscale*, 2016, **8**, 15774

Breakdown current density in *h*-BN-capped quasi-1D $TaSe_3$ metallic nanowires: prospects of interconnect applications†

Maxim A. Stolyarov,‡[a] Guanxiong Liu,‡[a] Matthew A. Bloodgood,[b] Ece Aytan,[a] Chenglong Jiang,[a] Rameez Samnakay,[a] Tina T. Salguero,[b] Denis L. Nika,[a,c] Sergey L. Rumyantsev,[d] Michael S. Shur,[d] Krassimir N. Bozhilov[e] and Alexander A. Balandin*[a]

We report on the current-carrying capacity of the nanowires made from the quasi-1D van der Waals metal tantalum triselenide capped with quasi-2D boron nitride. The chemical vapor transport method followed by chemical and mechanical exfoliation were used to fabricate the mm-long $TaSe_3$ wires with the lateral dimensions in the 20 to 70 nm range. Electrical measurements establish that the $TaSe_3$/*h*-BN nanowire heterostructures have a breakdown current density exceeding 10 MA cm^{-2}—an order-of-magnitude higher than that for copper. Some devices exhibited an intriguing step-like breakdown, which can be explained by the atomic thread bundle structure of the nanowires. The quasi-1D single crystal nature of $TaSe_3$ results in a low surface roughness and in the absence of the grain boundaries. These features can potentially enable the downscaling of the nanowires to lateral dimensions in a few-nm range. Our results suggest that quasi-1D van der Waals metals have potential for applications in the ultimately downscaled local interconnects.

Received 28th April 2016,
Accepted 9th August 2016

DOI: 10.1039/c6nr03469a

www.rsc.org/nanoscale

Recently discovered unique electrical,[1,2] thermal[3,4] and optical[5–7] properties of graphene have stimulated the search for other two-dimensional (2D) atomic crystals and heterostructures with properties distinct from the corresponding bulk materials.[8–16] A large number of the 2D materials belong to the family of transition metal chalcogenides that contain weak van der Waals bonding between the structural units.[17,18] Most research up to now has used the dichalcogenide compositions MX_2 (where M = Mo, W, Ta and other transition metals; X = S, Se, Te), such as MoS_2, $TaSe_2$, TaS_2 and related materials characterized by 2D layered structure.[19–27] Another class of the transition metal chalcogenides the trichalcogenides – exhibits quasi-1D crystalline structures. The examples include TiS_3, $TaSe_3$, TaS_3 and $NbSe_3$.[28–31] The crystal structure views of the monoclinic tantalum triselenide ($TaSe_3$) in Fig. 1(a) illustrate the main features of this material. Trigonal prismatic $TaSe_3$ forms the continuous chains that extend along the *b* axis, leading to fiber- or needle-like crystals with anisotropic metallic properties. These chains are arranged in the corrugated bilayer sheets indicated by the blue and yellow rows of prisms in Fig. 1(a). The van der Waals bonding between the sheets is weak, which allows the MX_3 materials to be exfoliated by the same mechanical methods as the MX_2 materials.

A study of the current-carrying capacity of exfoliated MX_3 materials is interesting from both fundamental science and practical applications points of view. A possibility of achieving very high breakdown current densities in quasi-1D metallic conductors may have implications for electronic industry. Indeed, continuous downscaling of the silicon (Si) complementary metal–oxide–semiconductor (CMOS) technology leads to increasing current densities in the copper (Cu) interconnects. According to the International Technology Roadmap for Semiconductors (ITRS), the present level of the current density, ~1.8 MA cm^{-2} at the half-pitch width of 28.5 nm will increase to ~5.35 MA cm^{-2} at the width of 7 nm.[32] There is

[a]*Nano-Device Laboratory (NDL) and Phonon Optimized Engineered Materials (POEM) Center, Department of Electrical and Computer Engineering, University of California – Riverside, Riverside, California 92521, USA. E-mail: balandin@ece.ucr.edu*
[b]*Department of Chemistry, University of Georgia, Athens, Georgia 30602, USA*
[c]*E. Pokatilov Laboratory of Physics and Engineering of Nanomaterials, Department of Physics and Engineering, Moldova State University, Chisinau, MD-2009, Republic of Moldova*
[d]*Department of Electrical, Computer and Systems Engineering, Rensselaer Polytechnic Institute, Troy, NY 12180, USA*
[e]*Central Facility for Advanced Microscopy and Microanalysis, University of California – Riverside, Riverside, California 92521, USA*

†Electronic supplementary information (ESI) available: Details of the material synthesis, device fabrication, transmission electron microscopy and diffraction. See DOI: 10.1039/c6nr03469a

‡These authors contributed equally to the project.

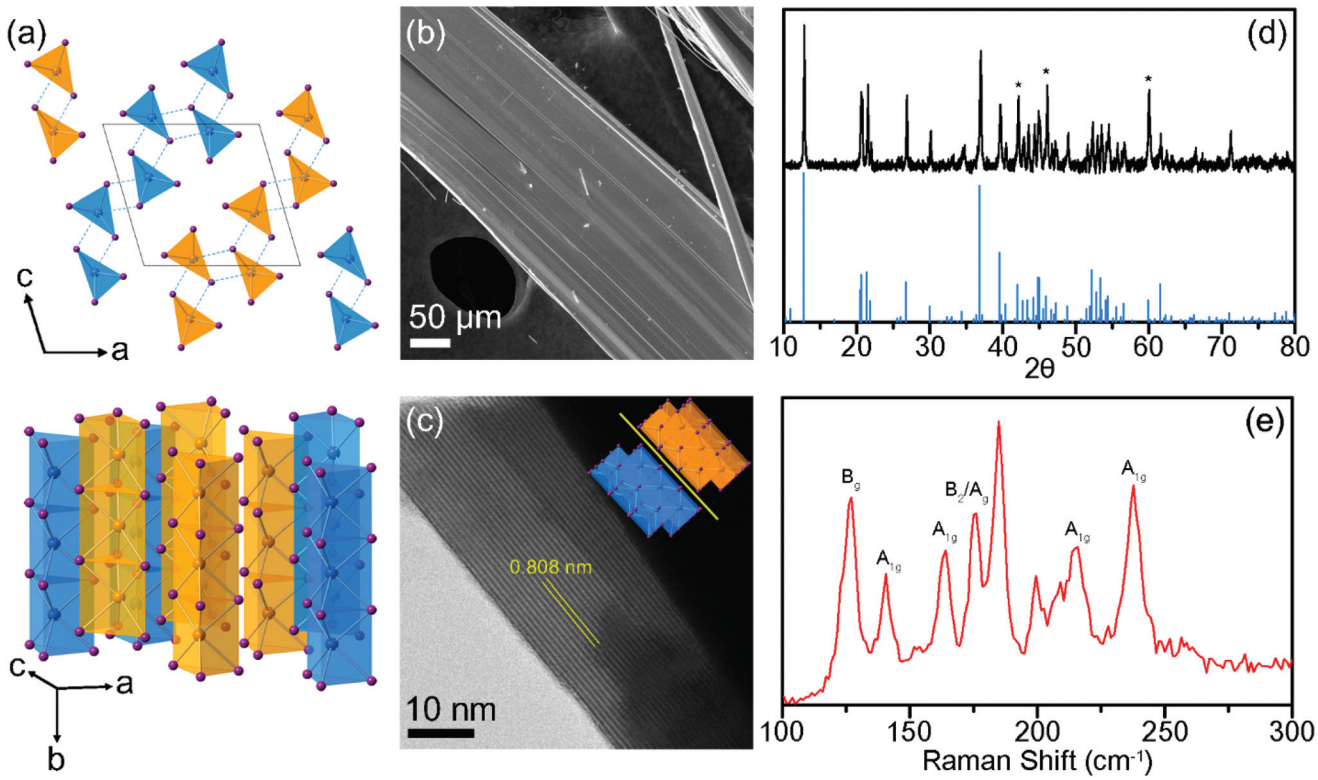

Fig. 1 (a) Crystal structure of monoclinic $TaSe_3$, with alternating corrugated layers of $TaSe_3$ colored blue and yellow. The top view shows the cross section of the unit cell, perpendicular to the chain axis (*b* axis), which highlights the van der Waals gaps within the material. The side view in the bottom panel emphasizes the 1D nature of $TaSe_3$ chains along the *b* axis. (b) SEM image of a $TaSe_3$ crystal used in this work. (c) HRTEM image of $TaSe_3$ after solvent exfoliation. The inset shows the position of the observed (1 0 −1) lattice plane in the van der Waals gap. (d) Powder XRD pattern of $TaSe_3$ crystals; the experimental data in black matches the reference pattern in blue (JCPDS 04-007-1143). The intensities of peaks marked with * are enhanced due to orientation effects. (e) Raman spectrum of $TaSe_3$ threads under 633 nm laser excitation.

no existing technology with the breakdown current density, J_B, high enough to sustain such currents. The ITRS projections indicate that the layer thicknesses will decrease from 57.0 nm currently in 2016 to 15.4 nm by 2028, while the interconnect cross-sectional area will scale down from 1624.5 nm^2 to 107.8 nm^2 over the same period of time. Scaling deep to the nanoscale range presents problems for conventional metals due to their polycrystalline structure, surface roughness and increased electrical resistivity owing to the electron–boundary scattering.[33] These factors motivate the search for alternative materials, which can complement Cu in selected areas, *e.g.* ultimately downscaled local interconnects.

In this Letter, we report results describing the current-carrying capacity of nanowires made from metallic $TaSe_3$ capped with hexagonal boron nitride (*h*-BN). This work establishes that quasi-1D $TaSe_3$ nanowires have the breakdown current density exceeding $J_B \sim 10$ MA cm^{-2}, which is an order-of-magnitude larger than that in Cu nanowires with diffusion barriers. In view of the promising current-carrying capacity of such quasi-1D/quasi-2D heterostructures and the possibility of ultimately downscaling their cross-sectional areas, we discuss the prospects of using quasi-1D metals as interconnects.

High-quality $TaSe_3$ crystals were prepared by the chemical vapor transport (CVT) method using iodine (see Methods). The morphology, crystalline structure, and phase purity of these crystals were characterized by scanning electron microscopy (SEM), electron dispersive spectroscopy (EDS), powder X-ray diffraction (XRD), and electron probe micro analysis (EPMA). Fig. 1(b) shows an SEM image of a representative fibrous $TaSe_3$ crystal ~225 μm wide and >10 mm long. The powder XRD pattern in Fig. 1(d) matches literature data for standard monoclinic $TaSe_3$ ($P2_1/m$),[31] albeit several peaks (marked with *) exhibit enhanced intensity due to the preferred orientation of particles within the powdered sample. Furthermore, both EDS and EPMA analyses (ESI†) show that the stoichiometry of the CVT-grown crystals is consistent with $TaSe_3$.

The crystals were subjected to successive chemical and mechanical exfoliation. The chemical exfoliation involved the low-power ultrasonic baths resulting in the dispersions containing the $TaSe_3$ "threads" of approximately 30 to 80 nm wide. Fig. 1(c) shows a high-resolution transmission electron microscopy (HRTEM) image of a $TaSe_3$ thread produced by exfoliation in ethanol. The clearly resolved lattice fringes with 0.808 nm separation are consistent with the (1 0 −1) interplanar distances of $TaSe_3$. As illustrated in the Fig. 1(c) inset, this plane occupies the van der Waals gap of the material, exactly between adjacent $TaSe_3$ sheets. In addition, the

HRTEM data shows no obvious structural defects. The electron diffraction patterns also confirm the crystallinity and orientation of the samples (see ESI†).

Micro-Raman spectroscopy further confirmed the quality of the exfoliated $TaSe_3$. The Raman measurements were performed in the backscattering configuration under λ = 633 nm laser excitation. Fig. 1(e) shows the Raman spectrum of a $TaSe_3$ thread under small-power excitation ($P \leq 0.5$ mW on the surface) in order to avoid local heating. Although the published Raman data for bulk $TaSe_3$ are limited[34] we were able to identify the main Raman peaks. The spectrum displays seven characteristic peaks in the 100 cm^{-1} to 300 cm^{-1} range that originate from the structure of the primitive monoclinic $TaSe_3$.[31,34,35] The peaks at 140 cm^{-1}, 164 cm^{-1}, 214 cm^{-1} and 238 cm^{-1} are attributed to the out-of-plane (A_{1g}) modes whereas the peaks at 176 cm^{-1} and 185 cm^{-1} correspond to the B_2/A_g vibrational modes, with B_2 and A_g designating vibrational symmetry in the chain and crystal respectively.[34] The peak at 127 cm^{-1} corresponds to the shear (B_g-like) vibrational mode.[34]

The overall analysis of the Raman, HRTEM and diffraction data indicates that the exfoliated $TaSe_3$ is single crystalline, as expected for the samples derived from the single crystalline CVT-grown material. Each $TaSe_3$ thread consists of the quasi-1D atomic-scale thread bundles based on the hierarchical structure of $TaSe_3$. Importantly, this complex structure disfavors the formation of grain structures within the thread, in contrast to the situation for conventional metals like copper with the face-centered cubic structures.[36–40] This feature is an important factor in downscaling the interconnect wires to a few-nm lateral cross-sections.

The $TaSe_3$ threads produced by chemical exfoliation were thinned further by mechanical exfoliation in a fashion similar to that typically used for graphene and MX_2 materials.[1,41,42] These $TaSe_3$ samples with very high aspect ratios were placed on the Si/SiO_2 substrates with pre-fabricated metal electrodes for a further characterization. Fig. 2(a) shows a representative SEM image of a millimeter long $TaSe_3$ nanowire with the lateral dimensions on the order of 50 nm placed on Ti/Au metal contacts. One can see in this image that the roughness of the metal contacts is larger than that of $TaSe_3$ nanowire. The thickness and roughness of the resulting nanowires were accurately determined *via* atomic force microscopy (AFM). The AFM inspection was used to examine the location and nature of the breakdown points after reaching J_B. Fig. 2(b) shows an AFM image of the nanowire region with the current induced damage. This nanowire did not have *h*-BN capping. It is clearly visible that the nanowire consists of multiple parallel crystalline threads.

In order to verify crystallinity and quality of nanowires along their entire length we performed the selective area electron diffraction (SAED) investigation of the nanowires along their length. Fig. 3 shows the diffraction patterns for five different locations confirming crystallinity and uniformity of the samples. The presence or absence of vacancies cannot be determined from these data, however. A more refined quality assessment is reserved for future studies.

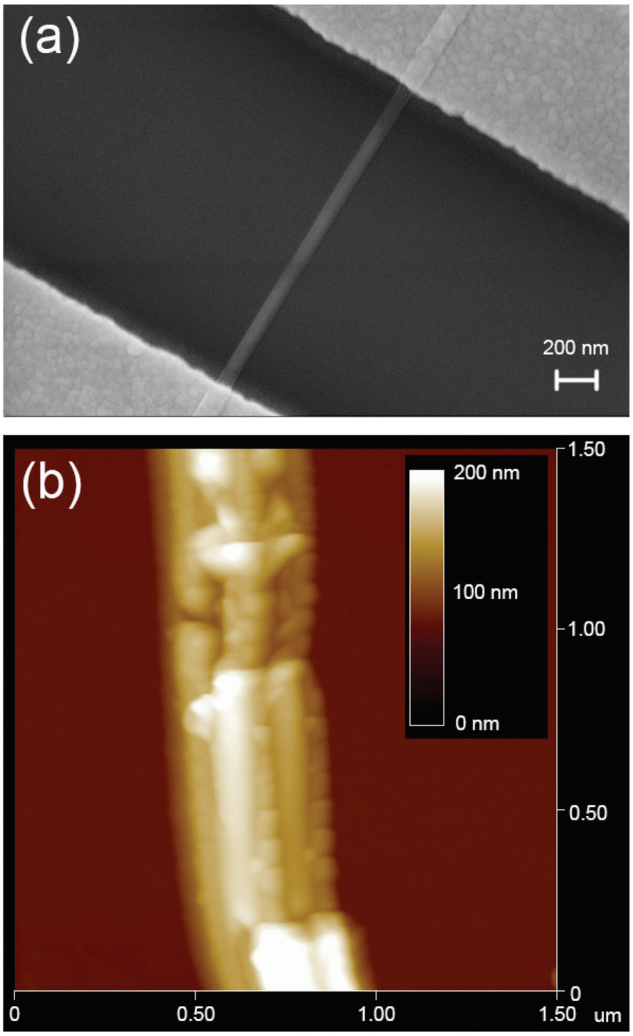

Fig. 2 (a) SEM image of a long $TaSe_3$ nanowire with the lateral dimensions on the order of 50 nm placed on top of the Ti/Au metal contacts. Note the much rougher surface of the conventional metal compared to the exfoliated $TaSe_3$ nanowire. (b) Atomic force microscopy image of the breakdown point in the $TaSe_3$ nanowire showing that the nanowires consist of multiple parallel crystalline threads.

The devices for testing the current-carrying capacity of the quasi-1D/quasi-2D $TaSe_3$/*h*-BN nanowire heterostructures were fabricated from the exfoliated $TaSe_3$ with the lateral cross-sections in the range 10 nm × 30 nm to 250 nm × 500 nm. Although it was possible to exfoliate nanowires with smaller thicknesses and widths, the selected samples allowed for the fabrication of better-quality metal contacts. To protect the exfoliated $TaSe_3$ nanowires from oxidation, we used an *h*-BN capping layer positioned on top of the quasi-1D channels. Capping MX_2 and MX_3 thin films with *h*-BN became the standard technique for fabricating high quality channels with Ohmic contacts. The protection with *h*-BN layer prevents oxidation and device degradation. We established that the uncapped devices did not have completely Ohmic characteristics and did not function as long as the capped devices. The

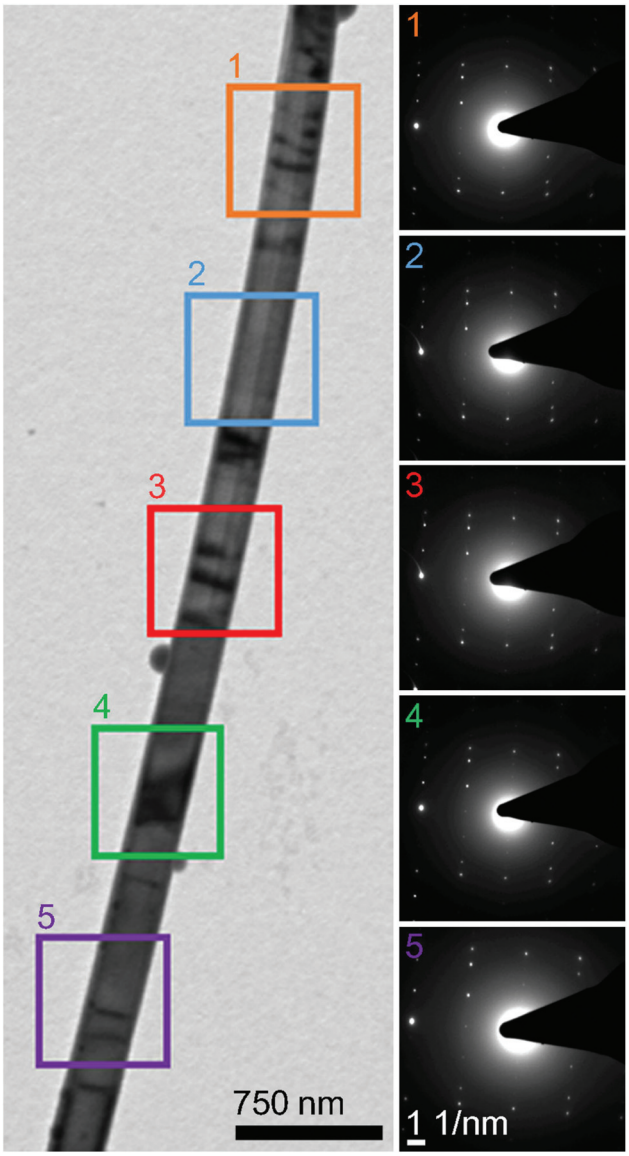

Fig. 3 Selective area electron diffraction data for five various locations along the length of the $TaSe_3$ nanowires confirming the crystallinity and uniformity of the sample.

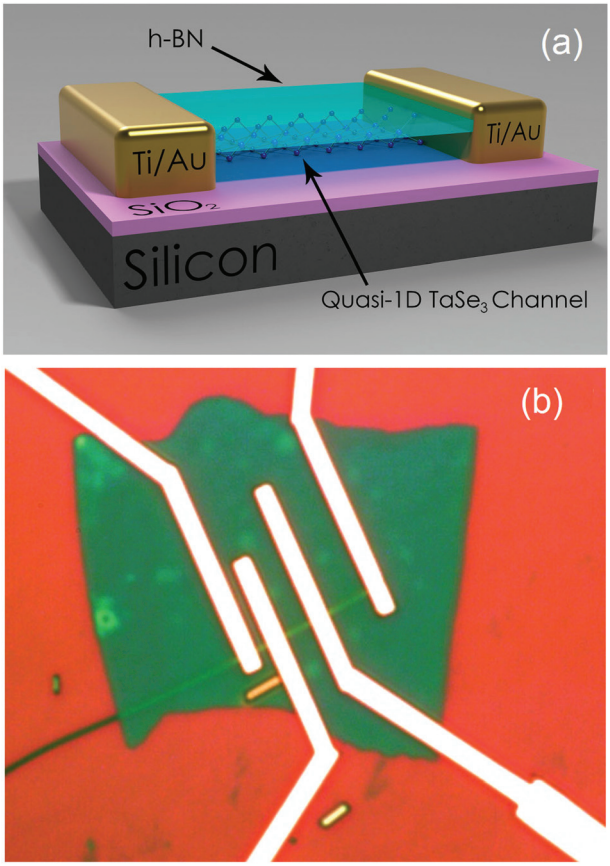

Fig. 4 (a) Schematic of the $TaSe_3$/*h*-BN quasi-1D/quasi-2D nanowire heterostructures used for the *I*–*V* and breakdown current density testing. (b) Optical microscopy image of a fabricated *h*-BN capped $TaSe_3$ nanowire sample. The pseudo colors are used for clarity. The metals tested for fabrication of Ohmic contacts included various combinations of thin layers of Cr, Ti, Au, Pd together with a thicker Au layer.

capped $TaSe_3$ nanowires were spin coated with the positive resist polymethyl methacrylate (PMMA) and heated two times. To expose the capped $TaSe_3$ nanowires, the assembled structures were selectively etched with sulfur hexafluoride (SF_6) gas on an inductively coupled plasma system (Oxford Plasmalab). The metal leads were deposited by the electron beam evaporation (Temescal BJD). We used different combinations of metals—10 nm (Cr, Ti, Au, Pd)/150 nm Au—in attempts to further improve the contacts. No major difference in performance with different metal contacts was observed. Fig. 4(a) shows the schematic of the fabricated devices. Fig. 4(b) presents an optical image of a representative device – prototype $TaSe_3$ interconnect with *h*-BN capping layer.

In our heterostructure design, *h*-BN, in addition to providing protection from oxidation, also facilitates heat dissipation from the quasi-1D channels owing to its high thermal conductivity, *K*.[43–45] There is significant discrepancy in the reported thermal data for *h*-BN bulk and thin films. The most commonly cited value is $K \approx 600$ W mK^{-1} along the basal plane at room temperature (RT).[45] This is substantially higher than the values for typical TMCs with MX_3 atomic composition, which are in the 3.5–30 W mK^{-1} range.[46–49] The SiO_2 layer under $TaSe_3$ is also thermally resistive with the thermal conductivity $K = 0.5 - 1.4$ W mK^{-1} at RT.[50] This is more than one hundred times smaller than that of Si, which has $K = 145$ W mK^{-1} in bulk form. For this reason, the *h*-BN capping layer in direct contact with $TaSe_3$ and metal electrodes creates an effective heat escape channel. The reduction of the $TaSe_3$ nanowire temperature should increase the breakdown current density by preventing electromigration or thermal breakdown.

Together with the quasi-1D/quasi-2D $TaSe_3$/*h*-BN heterostructures, we fabricated several devices without the *h*-BN capping. Some $TaSe_3$ samples had a larger width in order to test possible differences in the quality of the metal contacts

and J_B values. The device structures for the transmission line measurements (TLM) of the contact resistances were also made. Overall, we tested about 50 devices to ensure reproducibility. The devices with *h*-BN capping had better Ohmic contacts. Fig. 5(a–c) presents the low-field current–voltage characteristics (*I–V*s), TLM resistance data and high-field *I–V*s near the breakdown point, respectively. One can see from Fig. 5(a) that the contacts are Ohmic. The contact resistance extracted from TLM data is $2R_C$ = 22 Ω μm (see Fig. 5(b)). The resistivity is 2.6–6.4 × 10^{-4} Ω cm. This is consistent with the reported data for bulk $TaSe_3$.[31] Fig. 5(c) shows the high-field *I–V*s with the breakdown current density J_B = 32 MA cm^{-2}. In this specific device the breakdown was gradual with only one critical point.

Table 1 presents a representative summary of the breakdown current densities in some of the tested devices. The devices listed in this table had the channel length *L* in the range from 2 μm to 13 μm. The surface roughness of as fabricated (not subjected to polishing) $TaSe_3$ channels determined *via* AFM inspection was in the range from ~0.2 nm to ~0.5 nm. The main conclusion from these data is that J_B values for quasi-1D $TaSe_3$ nanowires capped with quasi-2D *h*-BN layers can exceed 10 MA cm^{-2}. The measured J_B = 32 MA cm^{-2} for a capped device with the thickness *H* = 20 nm is a factor of 18 higher than that in state-of-the-art Cu interconnect technology. The *h*-BN capped devices typically had higher J_B. The uncapped $TaSe_3$ device with J_B = 10 MA cm^{-2} had the smoothest surface with the roughness of ~0.2 nm. The increase in the width of $TaSe_3$ channel (changed *H*/*W* ratio) or the use of different metals did not produce major differences in the current-carrying capacity of the nanowires.

In approximately half of all devices we observed an unusual type of breakdown: an abrupt step-like decrease of the current (see Fig. 6(a and b)). Since different metal contacts have been used, *e.g.* Cr/Au and pure Au, it is clear that the step-like breakdown is intrinsic to the quasi-1D $TaSe_3$ nanowires. We attributed this type of breakdown to the atomic thread bundle structure of the nanowires. The atomic threads break down one by one or group by group. The result is analogous to severing some of the conducting channels connected in parallel. After the first break, the current abruptly goes down, then starts increasing again with the increasing voltage until the next atomic thread or bundle breaks (see Fig. 6(a)). Interestingly, in a few devices, we observed the abrupt increase in the current after the first break, which cannot be explained by an increased voltage (see Fig. 6(b)). This is likely related to reconnection of individual threads in the high current density regime.

Attempting to clarify the mechanism of the breakdown – thermal *vs.* electromigration – we conducted pulse measurements using a few devices with *h*-BN capping. The pulse characteristics were measured at RT using 10 μs voltage pulses. The pulse shape is shown in Fig. 7(a). The results of the measurements are provided in Fig. 7(b). For comparison, the low-voltage DC characteristics for the same device are also shown. One can see that the slopes of the DC and pulse characteristics coincide. The pulse characteristic remains

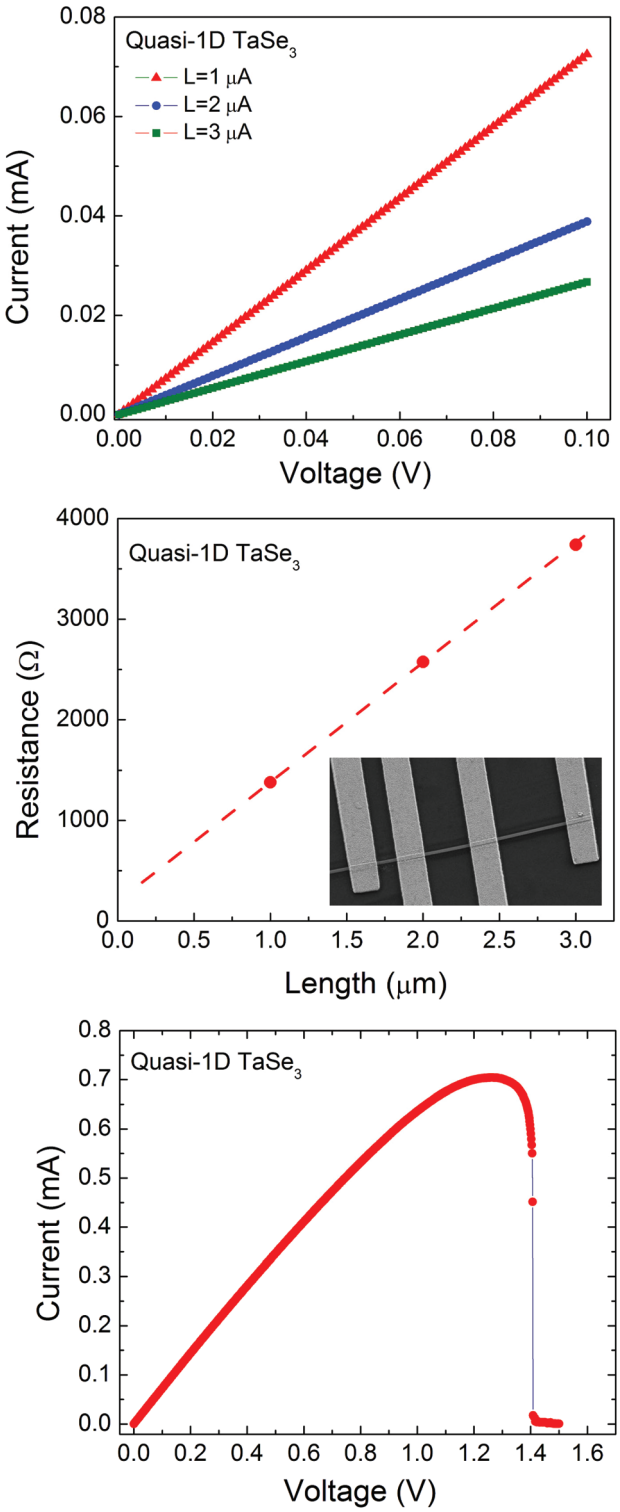

Fig. 5 (a) Low-field *I–V* characteristics of $TaSe_3$/*h*-BN quasi-1D/quasi-2D nanowire hetero-structures indicating that the contacts are Ohmic. (b) Transmission line measurement resistance data. (c) High-field *I–V* characteristics showing the breakdown point. In this specific device the breakdown is gradual. The inset shows a SEM image of the TLM structure used in the low-field testing.

Table 1 Breakdown current density in $TaSe_3$ nanowires and $TaSe_3$ /*h*-BN heterostructures

Sample	Width (nm)	Thickness (nm)	Current density (MA cm^{-2})	Comments
A1	110	20	32	BN capped
A2	320	80	11	BN capped
B1	75	34	10	No capping
B2	75	62	4	No capping
B3	75	40	6	BN capped

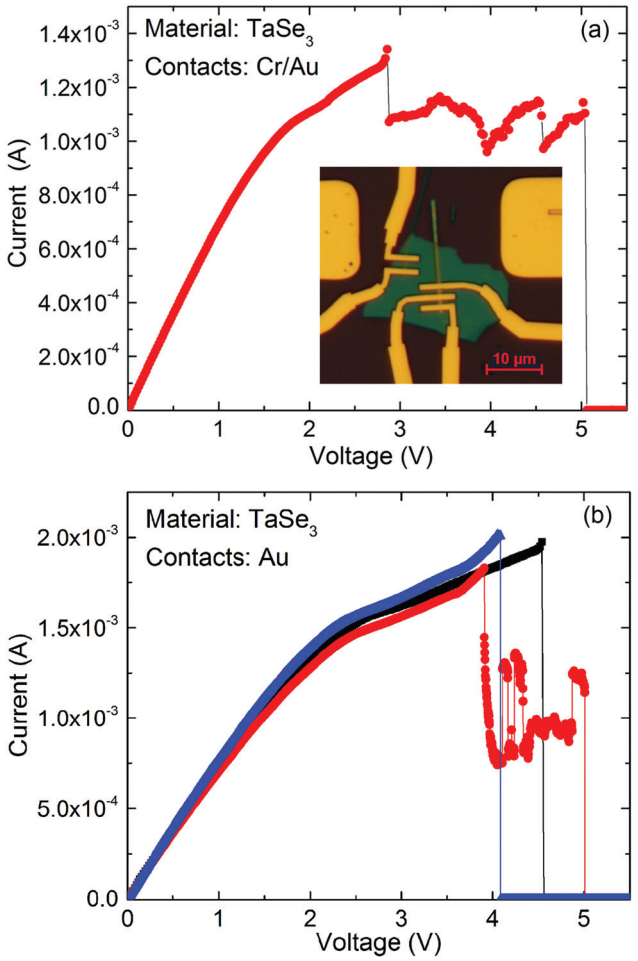

Fig. 6 (a) Current–voltage characteristics of a device with Cr/Au (10/150 nm) contacts. Note a step-like breakdown starting at $J_B = 4 \times 10^6$ A cm^{-2}. (b) Current–voltage characteristics of devices with pure Au contacts (150 nm) showing the step-like breakdowns at $J_B = 6.1 \times 10^6$ A cm^{-2} (black), 5.7×10^6 A cm^{-2} (blue), and 6.3×10^6 A cm^{-2} (red). The observed step-like breakdown was attributed to the quasi-1D atomic thread crystal structure of the material. The inset shows a microscopy image of a representative *h*-BN capped $TaSe_3$ nanowire device used in testing. The blue colored region in the image is *h*-BN layer.

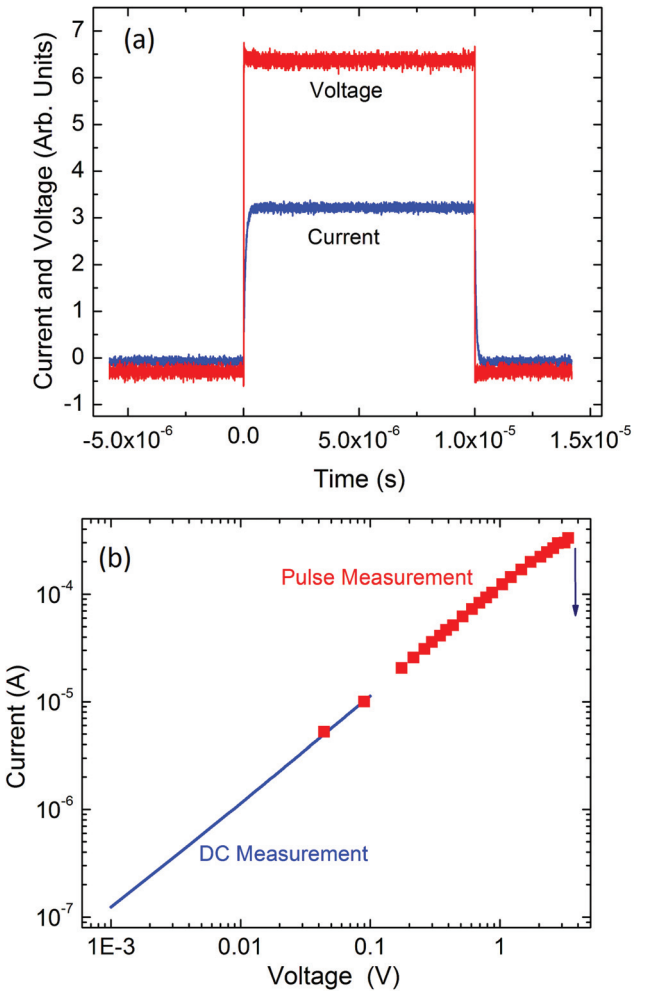

Fig. 7 (a) Duration and shape of the pulses applied to the *h*-BN capped $TaSe_3$ nanowire devices. (b) Current–voltage characteristics of the devices measured in pulse regime. The linear section correspond to DC characteristics for the same device.

nearly linear up to the breakdown point. The electrical field at the breakdown point in the pulse regime is consistent with the one obtained in DC measurements. This fact together with coincidence of the pulse and DC characteristics suggest that self-heating does not play a major role in the breakdown. The electromigration induced breakdown can also explain possible reconnection of some individual threads at high current density regime observed in Fig. 6(b). One should note that the characteristic switching times in conventional CMOS transistors are on the order of ns to ps. Hence, the high current lasts for only about this time in the integrated circuit. Possibly, at very short pulses, the breakdown will not develop until even higher current density than the obtained values.

These experiments have demonstrated the promise of quasi-1D $TaSe_3$ in terms of breakdown current density. In order to assess the potential of the quasi-1D metals for interconnect applications, we compare our results with the estimated electrical resistivity of Cu wires with nanometer-scale cross-sections. The electrical resistivity of Cu nanowires increases with the decreasing cross-section due to the electron scatterings on grains and nanowire boundaries. Using the Fuchs–Sondheimer model for the electron–nanowire surface scattering and the Mayadas–Shatzkes model for the electron–

grain boundary scattering, the electrical resistivity of metallic nanowires can be written as:[33,51–54]

$$\rho = \rho_0 \left[2C\lambda_0 \cdot (1-p) \cdot \left(\frac{1}{H} + \frac{1}{W} \right) + \frac{1}{1 - 3\alpha/2 + 3\alpha^2 - 3\alpha^3 \ln(1+1/\alpha)} \right] \quad (1)$$

where ρ_0 is the bulk electrical resistivity, W is the nanowire width, H is the nanowire thickness, λ_0 is the bulk electron mean free path (MFP), C = 1.2 is the constant for rectangular nanowire,[54] p is the specularity parameter determining strength of the electron – nanowire surface scattering, $\alpha = \lambda_0 \cdot R/(d_G \cdot (1-R))$, R is the reflectivity parameter of the electron – grain boundary scattering and d_G is the average grain size. The first term in eqn (1) describes the electron scattering on nanowire surface roughness while the second term corresponds to the electron scattering on grains. The values of the empirical parameters p and R change between 0 and 1. The specularity parameter p = 0 corresponds to the pure diffusive electron scattering on the nanowire surfaces with maximum resistance to the electron transport, while p = 1 corresponds to the pure specular scattering of electrons without adding any resistance to the electron transport. In this model, R = 1 corresponds to the strongest scattering of electrons on grains without reflection and R = 0 corresponds to the total electron reflection without scattering.

Fig. 8 shows the calculated electrical resistivity of Cu nanowires normalized to the bulk resistivity ρ_0 as a function of the nanowire width W for the case $H = W$. The results are shown for a range of parameters p and R reasonable for Cu.[33] As one can see, the electrical resistivity of Cu nanowires with W < 10 nm can increase by a factor of 50 to 300 compared to the bulk value. The resistivity increase by a factor of 100 makes it comparable with the values measured for quasi-1D $TaSe_3$ in this work. Because the relevant material parameters for $TaSe_3$ are not known, we cannot provide a direct comparison of resistivity scaling between Cu and $TaSe_3$. However, it is reasonable to expect a slower increase in the resistivity of quasi-1D van der Waals metals with decreasing cross-section area. In addition, since HRTEM and diffraction data indicate that the $TaSe_3$ samples examined in this work are single crystalline rather than polycrystalline, the possibility of electron scattering on grain boundaries is eliminated (see eqn (1)). The van der Waals nature of the bonds between the atomic threads should result in much smoother boundaries than found in conventional metals.

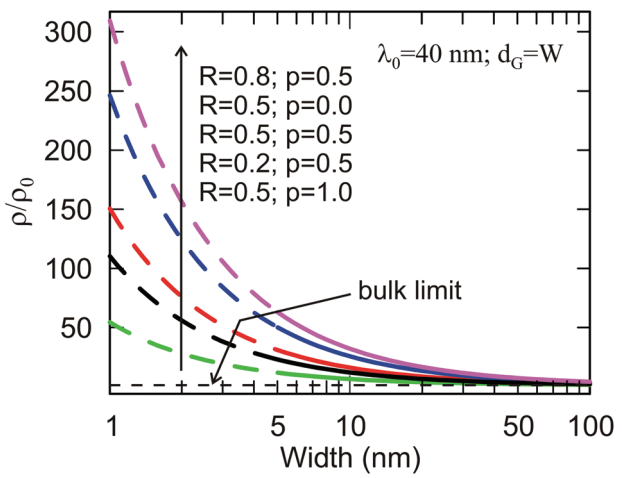

Fig. 8 Calculated electrical resistivity of Cu nanowires normalized to the bulk Cu resistivity as a function of the nanowire width W. The results are shown for a range of specularity parameters p, which defines electron scattering from nanowire surfaces and parameter R, which determines the electron scattering from grain boundaries. Note a strong increase in Cu resistivity as the lateral dimensions approach a few-nm range. The increase in $TaSe_3$ resistivity is expected to be less drastic owing to the absence of grain boundaries ($R \rightarrow 0$) and smoother surfaces ($p \rightarrow 1$).

The electrical current breakdown in thin metallic films is typically of electromigration nature.[49] In some materials, such as carbon nanotubes or graphene, characterized by strong sp^2 carbon bonds, the breakdown is thermally induced.[50] There are three types of diffusion processes caused by electromigration: bulk diffusion, grain boundary diffusion and surface diffusion. The grain boundary diffusion is the dominant process in aluminum interconnects whereas surface diffusion limits the breakdown current density in copper interconnects. Since HRTEM and other material characterization studies confirmed the single crystal nature of our $TaSe_3$ nanowires, one can rule out grain boundary diffusion as the failure mechanism. The dominance of the surface diffusion as the breakdown mechanism suggests that reducing the surface roughness of the nanowire, *e.g.* by chemical or mechanical polishing, can further increase J_B. The microscopy inspection of the breakdown points indicate that they are not located at the $TaSe_3$–metal contacts but rather distributed along the length of the nanowire. This means that the electron transport is diffusive rather than ballistic. Improving heat removal with the use of thermally conductive substrates, in addition to *h*-BN capping, can also benefit the current-carrying capacity of quasi-1D van der Waals metals.

In conclusion, we investigated the breakdown current density, J_B, of $TaSe_3$/*h*-BN quasi-1D/quasi-2D nanowire heterostructures. It was established that quasi-1D $TaSe_3$ nanowires have J_B exceeding 10 MA cm^{-2}—an order-of-magnitude higher than that in Cu. The quasi-1D single crystal nature of $TaSe_3$ results in the absence of grain boundaries, low surface roughness, and it potentially can allow for extreme downscaling to the few-nm range, enabling downscaled local interconnects.

Methods

Material preparation

$TaSe_3$ was synthesized directly from the elements. Tantalum (12.0 mmol, STREM 99.98% purity) and selenium (35.9 mmol, STREM 99.99% purity) were first mixed together. Then iodine (~6.45 mg cm^{-3}, J. T. Baker, 99.9% purity), followed by the tantalum + selenium mixture, was placed in a 17.78 × 1 cm fused quartz ampule (cleaned overnight in a nitric acid soak followed

by 12 h anneal at 900 °C). The ampule was evacuated and backfilled with Ar three times while submerged in an acetonitrile/dry ice bath. After flame sealing, ampules were placed in a Carbolite EZS 12/450B three-zone horizontal tube furnace heated at 20 °C min^{-1} to a final temperature gradient of 700–680 °C (hot zone–cool zone). The reaction was held at these temperatures for two weeks, then allowed to cool to room temperature. The $TaSe_3$ crystals were removed from the ampule and any remaining I_2 removed by sublimation under vacuum. Isolated yield of silver-black crystals was 90.8%. For chemical exfoliation, 6 mg of bulk powdered $TaSe_3$ crystals were sonicated in 10 mL ethanol for several hours. This resulted in a brownish-black non-transparent mixture. The mixture was centrifuged at 2600 rpm for 15 min to remove the larger particles. The remaining dispersed $TaSe_3$ threads were 30 to 80 nm wide.

Contributions

A. A. B. conceived the idea, coordinated the project, contributed to experimental data analysis and wrote the manuscript; T. T. S. supervised material synthesis and contributed to materials analysis; G. L., M. S., and R. S. performed mechanical exfoliation, fabricated and tested devices; M. A. B. synthesized $TaSe_3$ and conducted materials characterization; E. A. performed chemical exfoliation and TEM analysis; C. J. performed exfoliation and AFM study; K. N. B. assisted with TEM measurements and data analysis; D. L. N. conducted numerical simulations; S. L. R. conducted pulse measurements; M. S. S. contributed to data analysis. All authors contributed to writing of the manuscript.

Acknowledgements

The device fabrication work and part of the material characterization conducted at UCR were supported, in part, by the Semiconductor Research Corporation (SRC) and Defense Advanced Research Project Agency (DARPA) through STARnet Center for Function Accelerated nanoMaterial Engineering (FAME). Material synthesis at UGA and part of the material characterization conducted at UGA and UCR were supported by the National Science Foundation's Emerging Frontiers of Research Initiative (EFRI) 2-DARE project: Novel Switching Phenomena in Atomic MX_2 Heterostructures for Multifunctional Applications (NSF 005400). The authors thank Edward Hernandez (UCR) for his help with the schematic of the device.

References

1 K. S. Novoselov, A. K. Geim, S. V. Morozov, D. Jiang, Y. Zhang, S. V. Dubonos, I. V. Grigorieva and A. A. Firsov, *Science*, 2004, **306**(5696), 666–669.
2 Y. B. Zhang, Y. W. Tan, H. L. Stormer and P. Kim, *Nature*, 2005, **438**(7065), 201–204.
3 A. A. Balandin, S. Ghosh, W. Z. Bao, I. Calizo, D. Teweldebrhan, F. Miao and C. N. Lau, *Nano Lett.*, 2008, **8**(3), 902–907.
4 A. A. Balandin, *Nat. Mater.*, 2011, **10**(8), 569–581.
5 C. Casiraghi, A. Hartschuh, E. Lidorikis, H. Qian, H. Harutyunyan, T. Gokus, K. S. Novoselov and A. C. Ferrari, *Nano Lett.*, 2007, **7**(9), 2711–2717.
6 R. R. Nair, P. Blake, A. N. Grigorenko, K. S. Novoselov, T. J. Booth, T. Stauber, N. M. R. Peres and A. K. Geim, *Science*, 2008, **320**(5881), 1308–1308.
7 K. F. Mak, J. Shan and T. F. Heinz, *Phys. Rev. Lett.*, 2011, **106**(4), 046401.
8 K. S. Novoselov, D. Jiang, F. Schedin, T. J. Booth, V. V. Khotkevich, S. V. Morozov and A. K. Geim, *Proc. Natl. Acad. Sci. U. S. A.*, 2005, **102**(30), 10451–10453.
9 K. I. Bolotin, K. J. Sikes, Z. Jiang, M. Klima, G. Fudenberg, J. Hone, P. Kim and H. L. Stormer, *Solid State Commun.*, 2008, **146**(9–10), 351–355.
10 X. Cui, G. H. Lee, Y. D. Kim, G. Arefe, P. Y. Huang, C. H. Lee, D. A. Chenet, X. Zhang, L. Wang, F. Ye, F. Pizzocchero, B. S. Jessen, K. Watanabe, T. Taniguchi, D. A. Muller, T. Low, P. Kim and J. Hone, *Nat. Nanotechnol.*, 2015, **10**(6), 534–540.
11 B. Radisavljevic, A. Radenovic, J. Brivio, V. Giacometti and A. Kis, *Nat. Nanotechnol.*, 2011, **6**(3), 147–150.
12 A. K. Geim and I. V. Grigorieva, *Nature*, 2013, **499**(7459), 419–425.
13 D. Teweldebrhan, V. Goyal and A. A. Balandin, *Nano Lett.*, 2010, **10**(4), 1209–1218.
14 P. Goli, J. Khan, D. Wickramaratne, R. K. Lake and A. A. Balandin, *Nano Lett.*, 2012, **12**(11), 5941–5945.
15 A. A. Balandin, *Nat. Nanotechnol.*, 2013, **8**(8), 549–555.
16 M. A. Stolyarov, G. X. Liu, S. L. Rumyantsev, M. Shur and A. A. Balandin, *Appl. Phys. Lett.*, 2015, **107**(2), 023106.
17 L. f. Mattheis, *Phys. Rev. B: Solid State*, 1973, **8**(8), 3719–3740.
18 J. A. Wilson and A. D. Yoffe, *Adv. Phys.*, 1969, **18**(73), 193–335.
19 A. Kuc, N. Zibouche and T. Heine, *Phys. Rev. B: Condens. Matter*, 2011, **83**(24), 245213.
20 K. F. Mak, C. Lee, J. Hone, J. Shan and T. F. Heinz, *Phys. Rev. Lett.*, 2010, **105**(13), 136805.
21 L. T. Liu, S. B. Kumar, Y. Ouyang and J. Guo, *IEEE Trans. Electron Devices*, 2011, **58**(9), 3042–3047.
22 Y. Ding, Y. L. Wang, J. Ni, L. Shi, S. Q. Shi and W. H. Tang, *Physica B*, 2011, **406**(11), 2254–2260.
23 K. K. Kam and B. A. Parkinson, *J. Phys. Chem.*, 1982, **86**(4), 463–467.
24 A. R. Beal, H. P. Hughes and W. Y. Liang, *J. Phys. C: Solid State Phys.*, 1975, **8**(24), 4236–4248.
25 J. A. Wilson, F. J. Disalvo and S. Mahajan, *Adv. Phys.*, 1975, **24**(2), 117–201.
26 Z. Yan, C. Jiang, T. R. Pope, C. F. Tsang, J. L. Stickney, P. Goli, J. Renteria, T. T. Salguero and A. A. Balandin, *J. Appl. Phys.*, 2013, **114**(20), 204301.

27 R. Samnakay, D. Wickramaratne, T. R. Pope, R. K. Lake, T. T. Salguero and A. A. Balandin, *Nano Lett.*, 2015, **15**(5), 2965–2973.
28 A. Lipatov, P. M. Wilson, M. Shekhirev, J. D. Teeter, R. Netusil and A. Sinitskii, *Nanoscale*, 2015, **7**(29), 12291–12296.
29 J. O. Island, M. Buscema, M. Barawi, J. M. Clamagirand, J. R. Ares, C. Sanchez, I. J. Ferrer, G. A. Steele, H. S. J. van der Zant and A. Castellanos-Gomez, *Adv. Opt. Mater.*, 2014, **2**(7), 641–645.
30 J. O. Island, M. Barawi, R. Biele, A. Almazan, J. M. Clamagirand, J. R. Ares, C. Sanchez, H. S. J. van der Zant, J. V. Alvarez, R. D'Agosta, I. J. Ferrer and A. Castellanos-Gomez, *Adv. Mater.*, 2015, **27**(16), 2595–2601.
31 E. Bjerkelund, J. H. Fermor and A. Kjekshus, *Acta Chem. Scand.*, 1966, **20**(7), 1836–1842.
32 *International Technology Roadmap for Semiconductors*, 2013.
33 W. Steinhogl, G. Schindler, G. Steinlesberger and M. Engelhardt, *Phys. Rev. B: Condens. Matter*, 2002, **66**(7), 075414.
34 T. J. Wieting, A. Grisel and F. Levy, *Mol. Cryst. Liq. Cryst.*, 1982, **81**(1–4), 835–842.
35 E. Bjerkelund and A. Kjekshus, *Acta Chem. Scand.*, 1965, **19**(3), 701–710.
36 V. Y. Gertsman, M. Hoffmann, H. Gleiter and R. Birringer, *Acta Metall. Mater.*, 1994, **42**(10), 3539–3544.
37 J. J. Yang, Y. L. Huang and K. W. Xu, *Surf. Coat. Technol.*, 2007, **201**(9–11), 5574–5577.
38 T. Q. Qiu and C. L. Tien, *J. Heat Transfer-Trans. ASME*, 1993, **115**(4), 842–847.
39 E. M. Zielinski, R. P. Vinci and J. C. Bravman, *J. Appl. Phys.*, 1994, **76**(8), 4516–4522.
40 P. Goli, H. Ning, X. S. Li, C. Y. Lu, K. S. Novoselov and A. A. Balandin, *Nano Lett.*, 2014, **14**(3), 1497–1503.
41 C. R. Dean, A. F. Young, I. Meric, C. Lee, L. Wang, S. Sorgenfrei, K. Watanabe, T. Taniguchi, P. Kim, K. L. Shepard and J. Hone, *Nat. Nanotechnol.*, 2010, **5**(10), 722–726.
42 K. J. Koski and Y. Cui, *ACS Nano*, 2013, **7**(5), 3739–3743.
43 E. K. Sichel, R. E. Miller, M. S. Abrahams and C. J. Buiocchi, *Phys. Rev. B: Solid State*, 1976, **13**(10), 4607–4611.
44 I. Jo, M. T. Pettes, J. Kim, K. Watanabe, T. Taniguchi, Z. Yao and L. Shi, *Nano Lett.*, 2013, **13**(2), 550–554.
45 L. Lindsay and D. A. Broido, *Phys. Rev. B: Condens. Matter*, 2011, **84**(15), 155421.
46 E. Guilmeau, D. Berthebaud, P. R. N. Misse, S. Hebert, O. I. Lebedev, D. Chateigner, C. Martin and A. Maignan, *Chem. Mater.*, 2014, **26**(19), 5585–5591.
47 A. V. Inyushkin, A. N. Taldenkov and V. V. Florentiev, *Synth. Met.*, 1987, **19**(1–3), 843–848.
48 J. W. Brill, C. P. Tzou, G. Verma and N. P. Ong, *Solid State Commun.*, 1981, **39**(2), 233–237.
49 B. M. Zawilski, R. T. Littleton, N. D. Lowhorn and T. M. Tritt, *Solid State Commun.*, 2010, **150**(29–30), 1299–1302.
50 T. Yamane, N. Nagai, S. Katayama and M. Todoki, *J. Appl. Phys.*, 2002, **91**(12), 9772–9776.
51 K. Fuchs, *Proc. Cambridge Philos. Soc.*, 1938, **34**, 100–108.
52 E. H. Sondheimer, *Philos. Mag. Suppl.*, 1952, **1**, 1.
53 A. F. Mayadas and M. Shatzkes, *Phys. Rev. B: Solid State*, 1970, **1**(4), 1382.
54 Q. Huang, C. M. Lilley, M. Bode and R. S. Divan, 8th IEEE conference on nanotechnology, 2008, pp. 549–552.